

Research Article

Numerical Simulation of Split-Hopkinson Pressure Bar Tests for the Combined Coal-Rock by Using the Holmquist–Johnson–Cook Model and Case Analysis of Outburst

Beijing Xie ^{1,2}, Dongxin Chen ^{1,2}, Hao Ding ^{1,2}, Guangyu Wang ^{1,2} and Zheng Yan^{1,2}

¹School of Emergency Management and Safety Engineering, China University of Mining and Technology, Beijing 100083, China

²Beijing Key Laboratory for Precision Mining of Associated Energy, China University of Mining and Technology, Beijing 100083, China

Correspondence should be addressed to Beijing Xie; bjxie1984@cumtb.edu.cn

Received 13 August 2020; Revised 30 October 2020; Accepted 16 November 2020; Published 2 December 2020

Academic Editor: Fengqiang Gong

Copyright © 2020 Beijing Xie et al. This is an open access article distributed under the Creative Commons Attribution License, which permits unrestricted use, distribution, and reproduction in any medium, provided the original work is properly cited.

In the coal and rock dynamic disasters, such as the rock burst, dynamic load damage often acts simultaneously on the combined coal and rock mass. Based on the split-Hopkinson pressure bar (SHPB) test of the combined coal and rock with a bullet velocity of 4.590–8.791 m/s, the numerical model of four kinds of combined coal and rock with different sandstone-coal-sandstone ratios, including 1:1:1, 2:1:1, 1:1:2, and 1:2:1, is investigated. A finite element software (LS-DYNA) and the Holmquist–Johnson–Cook (HJC) constitutive model of rock are employed in these regards. The stress waveform, the oscillation phenomenon of stress wave, and the damage process of the specimen in the impact test of the composite coal and rock are studied. The obtained results show that the compression-shear failure is the main failure mode of the coal body and the tensile failure of the sandstone along the axial direction in the composite coal-rock specimens. Moreover, it is found that combination of coal and rock samples is mainly destroyed by the coal body, which has no correlation with the impact speed and combination mode. Finally, numerical simulation about Hongling coalmine extralarge tunnel malfunction is carried out. Obtained results showed the protruding and stress change processes of the coal seam of the tunnel exposing. It is found that the simulation results are in an excellent agreement with those from the field investigation. The present study may provide a reference for further understanding the mechanism of the coal and rock dynamic disasters, such as the rock burst.

1. Introduction

Studies show that as the coal mining depth increases, the geostress and gas pressure increase significantly, and the geological occurrence becomes very complicated. Moreover, the coal-rock dynamic disasters, such as the impact pressure and coal and gas outburst, increase [1]. The coal seams are deposited underground in the form of coal-rock interbeds [2]. However, these seams are not separately distributed, and they may be connected to each other. Investigating different mining methods for various working conditions showed that the coal body itself is destroyed during the mining process, and the rock mass adjacent to the top and bottom plates is damaged. It is found that this results in the overall instability of the coal-rock interbed [3]. Therefore, the interaction

between rocks and coal seams should be considered during the mining process [4]. In recent years, studying the dynamic and static mechanical parameters of the combined coal-rock has been widely concerned by many researchers. Liu et al. [5] carried out uniaxial compression experiments on 13 coal-rock combinations and found that the compressive strength of coal samples increases as the rock strength increases while it decreases as the coal-rock height ratio increases. Guo et al. [6] found that the tensile strength of the layer-crack structure decreases as the fissure length (or width) increases through uniaxial compression and Brazilian tests. Chen et al. [7] conducted an experiment on the deformation and destruction behavior of coal-rock combinations under the uniaxial compression. They found that mechanical properties and deformation-destructive

characteristics of the coal-rock composites are mainly depend on the coal composition and its percentage in the coal-rock. Gong et al. [8] studied the effect of low loading rate on the mechanical behavior of coal-rock combined body. Moreover, Gong et al. [9] used a split-Hopkinson pressure bar (SHPB) device to perform high strain rate dynamic compression tests on a variety of coal-rock combinations. They showed that the dynamic stress-strain curve of the coal-rock has double peak characteristics in the high loading rates. Zhao et al. [10] employed the FLAC3D software to simulate and study the damage evolution of the coal-rock with different combinations. They found that the overall damage rate increases as the coal seam thickness increases. Furthermore, Fu et al. [11] employed the RFPD 2D software to numerically investigate the mechanical properties and acoustic emission characteristics of coal-rock under different confining pressures and dip angles. They concluded that the stress-strain curves of different coal-rock combinations are similar, and the peak strength is close to the uniaxial compressive strength of the coal. Reviewing the literature indicated that majority of studies on the mechanical characteristics of the coal-rock with different combinations are focused on static or slow loading conditions [5–11]. In other words, the dynamic mechanical properties of coal-rock with different combinations under the impact loading have not been deeply studied yet.

Recently, the SHPB has been widely used for studying the dynamic mechanical properties of materials [12] and has achieved reasonable results in soft materials [13, 14], metallic materials [15, 16], and brittle materials [17, 18]. The improved SHPB test device can be utilized to study the dynamic mechanical properties of materials for different conditions [19, 20]. Doan and Billi [21] investigated the high strain rate behavior of unconfined Carrara marble through a set of experiments with a split-Hopkinson pressure bar. Zhang et al. [22] made discussion and comparisons on the dynamic fracture processes and specimen fragments in the clay brick to explain the dynamic enhancement in brick mechanical properties. Gong et al. [23] obtained the effects of high strain rates and low confining pressures on the dynamic mechanical properties of sandstone experimentally with a modified triaxial SHPB system. However, due to the limitations in test equipment and experimental methods, there are not enough experimental research studies on the impact damage of the coal and rock. On the contrary, numerical methods can resolve the problems. Through numerical simulation, the stress and strain variations inside the coal-rock can be calculated. Therefore, the propagation and damage characteristics of stress waves in the coal and rock can be analyzed, and the limitations in the laboratory analysis of the dynamic load are covered. Holmquist et al. [24] proposed the Holmquist–Johnson–Cook (HJC) constitutive model for the concrete and rock under high strain rate and large deformation problems. The HJC model has been used for dynamic failure analysis of the coal and rock, and it has achieved satisfactory results [25, 26] considering the mechanical similarity between the coal and rock and the ordinary rock and concrete materials. They utilized the concrete HJC constitutive model to investigate coal samples

and simulated the damage process of coal samples under different impact velocities. They showed that the numerical results are in a good agreement with those from the experiment. Li et al. [26, 27] used the HJC constitutive model and commercial finite element software, called LS-DYNA, to numerically investigate the coal-rock SHPB test and the coal-rock SHPB passive confining pressure test. They found that the simulation results have a good similarity with the experimental results.

In order to explore the evolution law of the combined impact damage of the coal-rock, it is intended to perform the SHPB test for different coal-rock combination ratios, including 1:1:1, 2:1:1, 1:1:2, and 1:2:1. Moreover, the LS-DYNA finite element analysis software and the HJC constitutive model are employed to construct the damage evolution and dynamic fracture process of the combined coal-rock in the dynamic impact test. Then, the feasibility and effectiveness of the HJC constitutive model will be verified by comparing the numerical simulation results with those from the experimental results. Because the previous research on the dynamic mechanical characteristics of combined coal-rock under impact load has not been carried out in depth, this paper studies the dynamic characteristics of coal-rock samples under instantaneous impact failure by taking the actual coal-rock composite structure under the impact load as the research object and further verifies with the actual case, so as to further study the dynamic mechanical characteristics. It is intended to provide an experimental basis for further understanding the occurrence mechanism of the coal-rock dynamic disasters, such as the rock burst, coalmine rock disaster monitoring, and early warning, which is of great significance from safety points of view.

2. SHPB Test Device

The combined coal-rock dynamic impact test is completed with the SHPB testing device of the China University of Mining and Technology (Beijing). It should be indicated that the SHPB device consists of a striker (bullet), an incident bar, and a transmission bar. This test device uses a special shaped double-cone spindle with a total length of 540 mm, where the cone ratio of the bullet is 310:100:130 [28]. The approximately half-sine loading wave was generated by the spindle-shaped bullet, which has been suggested as the ideal loading waveform for SHPB testing device [29, 30]. It should be indicated that this shape of the loading wave is more suitable for the dynamic test of the coal-rock brittle materials [31]. The specific size of the bullet is shown in Figure 1.

In the experiment, the “top-coal-base” composite coal-rock sample MY1–MY23 was produced. It should be indicated that the MY6 test failed. A total of 22 impact compression tests are carried out in the present study, with sample height ratios of 1:1:1 (MY1–MY5), 2:1:1 (MY7–MY12), 1:1:2 (MY13–MY18), and 1:2:1 (MY19–MY23). In order to minimize the inertia effect of the test piece and satisfy the internal stresses, it is assumed that all samples are uniform [32]. According to the best aspect ratio calculation recommended by Davies and Hunter [33],

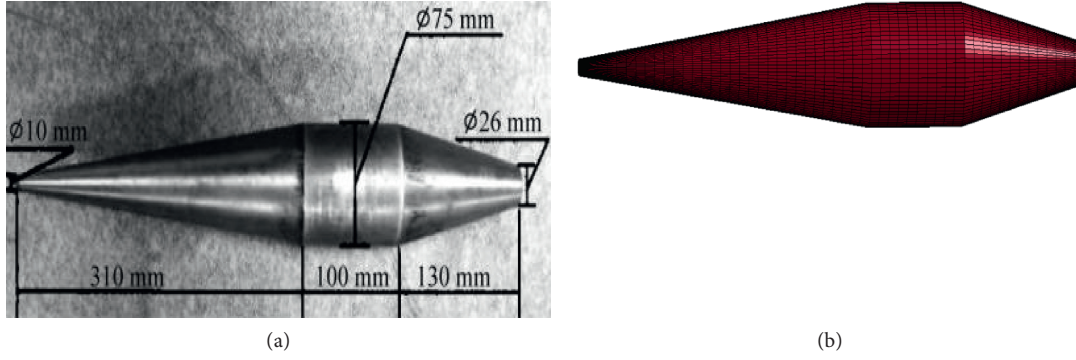


FIGURE 1: Experimental spinning cone bullet: (a) spindle-shaped bullet; (b) spindle-shaped bullet model.

the diameter, length, and the aspect ratio of the coal-rock cylindrical specimen are set to $D = 75$ mm, $L = 40$ mm, and $L/D = 8/15$, respectively [26]. Moreover, in order to reduce the influence of the interface friction during the test, the Vaseline lubrication is applied between the elastic bar and the test piece interface [34]. Figure 2 shows configurations of different experimental combined coal-rock samples.

Combined with the physical parameters of the actual pressure bar, both the incident bar and the transmission bar adopt a linear elastic model of steel material, where the diameter, length, and density are 75 mm, 2000 mm, and $\rho = 7800$ kg/m³, respectively. Moreover, the elastic modulus and Poisson's ratio are $E = 206$ GPa and $\nu = 0.36$, respectively. Finally, the impact velocity v is 4.590 to 8.791 m/s, and the specific experimental data are shown in Table 1 [31].

3. Material Model and Parameter Selection

3.1. HJC Dynamic Constitutive Model. As shown in Figure 3, the HJC constitutive equation uses a three-stage polynomial equation of state to describe the relationship between the coal-rock pressure (p) and the volumetric strain (μ), in the elastic phase (OA segment), plastic phase (AB segment), and the dense compaction phase of the material (BC segment) [24]. These phases are described in the following:

- (1) Elastic phase ($p_w < p_c$): the hydrostatic pressure (p_w) of the material has linear correlation with the volumetric strain (μ) of the material:

$$p_w = K_e \mu, \quad (1)$$

where $K_e = R'_c / 3(1 - 2\nu)$ and ν are the bulk modulus of the material and Poisson's ratio of the coal sample, respectively [31].

- (2) Plastic phase ($p_c \leq p_w \leq p_l$): in this phase, the hydrostatic pressure is calculated from the following equation:

$$p_w = p_l + \left(\frac{(p_l - p_c)(\mu - \mu_l)}{(\mu_l - \mu_c)} \right), \quad (2)$$

where μ_l , μ_c , and p_l are the compacted volume strain corresponding to the compaction pressure, crushed volume deformation of the material during the uniaxial compression, and the compaction pressure, respectively.

In the unloading section, the governing equations are

$$p_w - p_{\max} = [(1 - F)K_e + FK_1](\mu_l - \mu_{\max}), \quad (3)$$

$$F = \left(\frac{(\mu_l - \mu_{\max})}{(\mu_l - \mu_c)} \right),$$

where K_1 denotes the plastic bulk modulus. Moreover, p_{\max} and μ_{\max} are the maximum volume pressure and volume strain achieved before unloading, respectively [24].

- (3) Completely compact phase ($p_w > p_l$): in the loading section, the hydrostatic pressure is calculated as

$$p_w = k_1 \bar{\mu} + k_2 \bar{\mu}^2 + k_3 \bar{\mu}^3, \quad (4)$$

$$\bar{\mu} = \left(\frac{(\mu - \mu_l)}{(1 + \mu_l)} \right),$$

where k_1 , k_2 , and k_3 are constants and $\bar{\mu}$ is the corrected volume strain.

In the unloading section,

$$p_w - p_{\max} = k_1 (\bar{\mu} - t \bar{\mu}_{\max}). \quad (5)$$

The HJC constitutive model uses the dynamic damage factor D to describe the damage of the material, which is expressed as the cumulative plastic strain and the volumetric strain:

$$D = \sum \frac{\Delta \varepsilon_p + \Delta \mu_p}{\varepsilon_p^f + \mu_p^f}, \quad (6)$$

$$\varepsilon_p^f + \mu_p^f = D_1 (P^* + T^*)^{D_2},$$

where $\Delta \varepsilon_p$ and $\Delta \mu_p$ are the equivalent plastic strain increment and plastic volume strain increment, respectively. Moreover, ε_p^f and μ_p^f are the equivalent plastic strain and plastic volume strain of the fracture under normal pressure, respectively. Furthermore, p^* , s , and T^* are the standardized



FIGURE 2: Configurations of different experimental coal-rock combination samples: (a) 1 : 1 : 1 (MY1–MY5); (b) 2 : 1 : 1 (MY7–MY12); (c) 1 : 1 : 2 (MY13–MY18); (d) 1 : 2 : 1 (MY19–MY24).

TABLE 1: Affecting statistics.

Velocity ($v/m \cdot s^{-1}$)	Specimen number	Specimen size $D \times L$ (mm \times mm)	Sandstone: coal: sandstone combination ratio	Maximum strain rate ($\dot{\epsilon}_{max}/s^{-1}$)	Destructive strain ($\epsilon_b/10^{-3}$)	Σ_{max} (Mpa)	Destruction
5.008	MY1	75 \times 40	1 : 1 : 1	126.97	10.2	12.70	Broken
5.712	MY2	75 \times 40	1 : 1 : 1	143.98	14.2	18.23	Broken
6.371	MY3	75 \times 40	1 : 1 : 1	162.56	12.2	21.98	Broken
6.754	MY4	75 \times 40	1 : 1 : 1	170.66	13.3	25.21	Broken
7.222	MY5	75 \times 40	1 : 1 : 1	173.48	16.4	30.06	Broken
4.590	MY12	75 \times 40	2 : 1 : 1	110.41	12.4	8.65	Broken
5.062	MY11	75 \times 40	2 : 1 : 1	121.93	10.7	10.64	Broken
6.136	MY10	75 \times 40	2 : 1 : 1	150.53	10.4	19.24	Broken
6.205	MY9	75 \times 40	2 : 1 : 1	150.07	9.8	24.43	Broken
7.165	MY8	75 \times 40	2 : 1 : 1	174.26	14.0	19.69	Broken
7.671	MY7	75 \times 40	2 : 1 : 1	184.01	16.3	35.28	Broken
6.660	MY13	75 \times 40	1 : 1 : 2	158.03	10.3	32.25	Broken
7.140	MY14	75 \times 40	1 : 1 : 2	179.00	10.5	11.78	Broken
7.584	MY15	75 \times 40	1 : 1 : 2	178.48	12.9	36.46	Broken
8.093	MY16	75 \times 40	1 : 1 : 2	195.49	10.4	17.75	Broken
8.022	MY17	75 \times 40	1 : 1 : 2	186.91	14.2	43.24	Broken
8.791	MY18	75 \times 40	1 : 1 : 2	192.42	11.8	23.34	Broken
5.880	MY23	75 \times 40	1 : 2 : 1	149.79	9.0	15.10	Broken
6.508	MY19	75 \times 40	1 : 2 : 1	162.62	8.0	15.30	Broken
7.054	MY20	75 \times 40	1 : 2 : 1	171.24	13.5	14.02	Broken
7.465	MY21	75 \times 40	1 : 2 : 1	182.30	12.4	22.41	Broken
8.200	MY22	75 \times 40	1 : 2 : 1	192.42	14.0	27.10	Broken

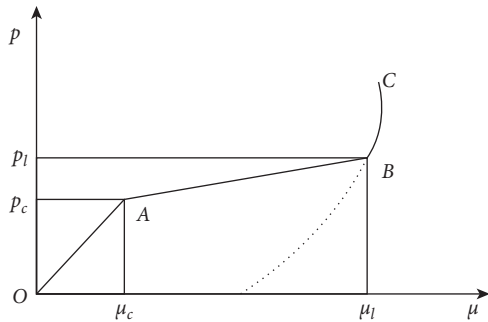


FIGURE 3: Pressure-volumetric strain curve of the HJC model.

hydrostatic pressure and the maximum tensile strength of coal and rock masses, respectively. Finally, D_1 and D_2 are damage constants [27].

3.2. Determination of Parameters of the Combined Coal-Rock HJC Material Model

3.2.1. *Determination of Parameters of Common Coal Materials.* In the LS-DYNA software, the HJC constitutive model is defined as the “*mat_johnson_holmquist_concrete,” which has 21 parameters. It should be indicated that model parameters of the coal material are selected in accordance with the Xie Beijing experiment [25]. Table 2 shows the selected parameters.

3.2.2. *Determination of Rock Material Parameters.* Because the stress-strain curve of sandstone and coal is very different [35], the relevant literature parameters were consulted to establish the sandstone material model [36]. It is intended to investigate the influence of the combination type and impact velocity changes in the simulation results. The

TABLE 2: Input parameters of the HJC model for the ordinary coal material.

ρ_0 (kg/m ³)	G (Pa)	f_c (Pa)	A	B	C	N	S_{\max}	D_1	D_2	$\epsilon_{f\min}$
1352	5.8E8	9E6	0.4	0.7	0.005	0.5	7.0	0.027	1.0	0.01
T (Pa)	p_c (Pa)	μ_c	p_l (Pa)	μ_l	k_1 (Pa)	k_2 (Pa)	k_3 (Pa)	$\dot{\epsilon}_0$	f_s	
1.86E6	3E6	8E-4	1E9	0.12	85E9	-17E10	208E9	60	0.04	

sandstone material parameters of the selected HJC constitutive model are shown in Table 3.

3.3. Establishment of the Finite Element Model. According to the actual size of the test, the bullet, pressure bar, and three-dimensional solid elements of the combined coal-rock specimen (Solid164) are established. Considering the structure symmetry, only a quarter of the test device and the test piece are modeled. Then, the model is meshed, and the bullet and the input and transmission bars are divided into 20 parts in the radial direction, 54 pieces in the axial direction of the bullet, and 200 parts in the axial direction of the incident and transmission bars. Moreover, the bullet and the pressure bar are divided into 1 part per 10 mm in the axial direction. In order to reflect the impact damage process of the combined coal-rock specimens more directly, the combined coal-rock specimens are finely meshed so that the combined specimens are divided into 20 parts in radial directions and the axial direction is divided into 1 mm long each, as shown in Figure 4. The bullet and the incident bar are in automatic contact with the surface and the erosion contact between the pressure bar and the test piece. By neglecting the friction between the contact surfaces, the contact algorithm of the penalty function is used to reduce the hourglass effect. It should be indicated that the value of the contact stiffness penalty function factor (f) is set to 2 [24]. Based on the actual SHPB test, the simulation is performed by applying the loading speed to the bullet directly. Due to the short length of rods and the combined coal-rock specimens in the SHPB test, the attenuation of the stress waves in the rod and the specimen is ignored in the simulation [37].

4. Numerical Simulation Results and Analysis

4.1. Waveform of Stress Waves. In this section, the stress waveform results of the combined coal-rock under some typical speeds are presented. Figure 5 shows the measured and simulated stress waveform curves at the middle of the incident and transmission bars at different speeds, including 5.008 m/s (combined coal MY1), 7.671 m/s (combined coal MY7), 6.660 m/s (combined coal-rock MY13), and 5.880 m/s (combined coal-rock MY23).

Figure 5 shows good consistency between simulated and measured stress waveform trends. It is observed that the incident wave grows in a stepwise manner. Focusing on the incidence wave, the measured peak values of the incidence wave at the four bullet speeds in the experiment are 101.96, 164.94, 133.46, and 132.26 MPa, respectively; the simulated peak values of the incidence wave measured by the corresponding four bullet speeds are 104.35, 165.10, 139.15, and 131.82 MPa, respectively. It is found that the peak value of

the simulated incidence wave is slightly higher than the peak value of the measured incidence wave, and there is little discrepancy between the two values. Since the propagation of the experimental stress wave in the bar decreases with time, the stress wave in the numerical simulation does not decrease. When the wave reaches interface between two different impedances, the wave reflection and transmission occur at the interface. When the stress wave reaches the transmission bar, it passes through three sections with different wave impedances and the incident wave reflection causes it to rise in three steps. However, the measured incident wave does not exhibit a stepwise growth because the stress-strain acquisition rate is low. Moreover, the end faces of the bars are flat in the numerical simulation, and the combined coal and rock specimens in the experiment inevitably have defects. This results in loss of stress wave during the wave propagation. Because of the nonuniformity in the coal-rock, the stress waveform in the experiment is different from that of the numerical simulation in terms of incident and reflected wave width and rise. Numerical simulation of the stress waveform is also associated with a certain oscillation phenomenon. However, the stress waveform distributions obtained from the numerical simulation and experiment are consistent with the overall trend of transmission wave rise. There are a lot of microcracks and micropores in the combined coal-rock, which will produce significant evolution damage under impact load, especially under the condition of medium and high strain rate. And the internal material of the combined coal-rock is not uniform. These factors make the stress-strain curve in Figure 6 fluctuate, but Figure 6 shows good consistency between simulated and measured stress-strain waveform trends. Because the simulation is carried out under ideal conditions, there are some differences due to small external interference. Although the simulated and measured values are slightly different, there are only minor differences. Therefore, the numerical simulation results can replace the experiments, which can be used to test and analyze the dynamic test of the combined coal-rock.

4.2. Dynamic Stress Equilibrium Curves. In order to obtain effective test data, the stress balance at both ends of the sample is achieved during the test, as shown in Figure 7.

Figure 7 shows the dynamic stress balance curves of the four specimens at the corresponding bullet speed. The stress-time curve of the interface between the incident rod and the sample (incident + reflection in the figure) is calculated from the incident signal plus the reflected signal; the stress-time curve of the interface between the transmission rod and the sample (transmission in the figure) is calculated by the transmission signal. It can be seen from the figure that the

TABLE 3: Input parameters of the HJC model for sandstone material.

ρ_0 (kg/m ³)	G (Pa)	f_c (Pa)	A	B	C	N	S_{max}	D_1	D_2	ϵ_{fmin}
2400	1.5E8	48E6	0.79	1.6	0.007	0.61	7.0	0.04	1.0	0.01
T (Pa)	p_c (Pa)	μ_c	p_l (Pa)	μ_l	k_1 (Pa)	k_2 (Pa)	k_3 (Pa)	$\dot{\epsilon}_0$	f_s	
4E6	16E6	0.001	0.8E9	0.1	85E9	-17E10	208E9	60	0.01	

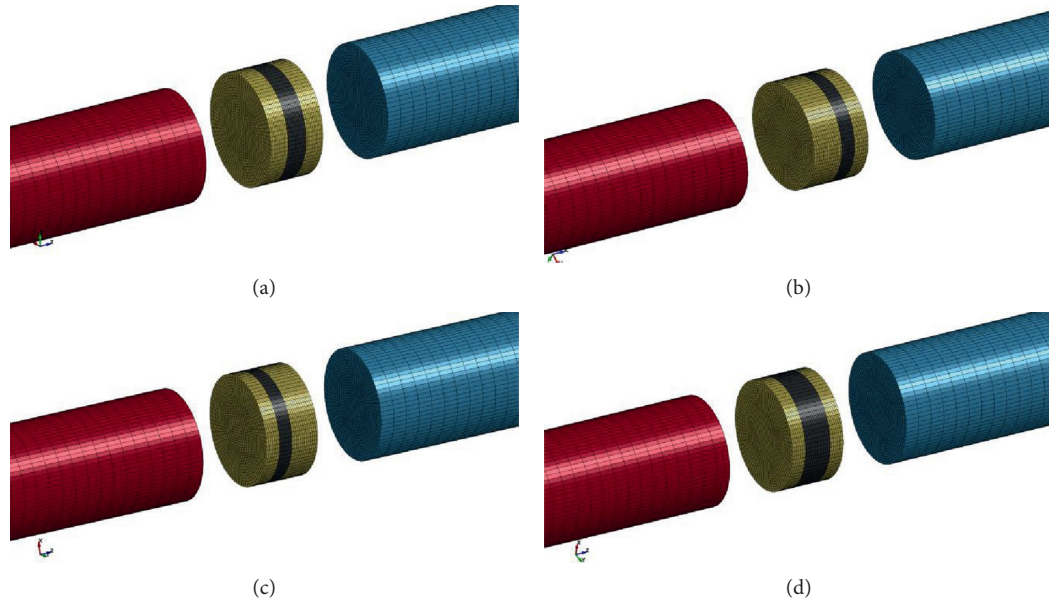


FIGURE 4: Configuration of the bar and sample grid: (a) 1:1:1; (b) 2:1:1; (c) 1:1:2; (d) 1:2:1.

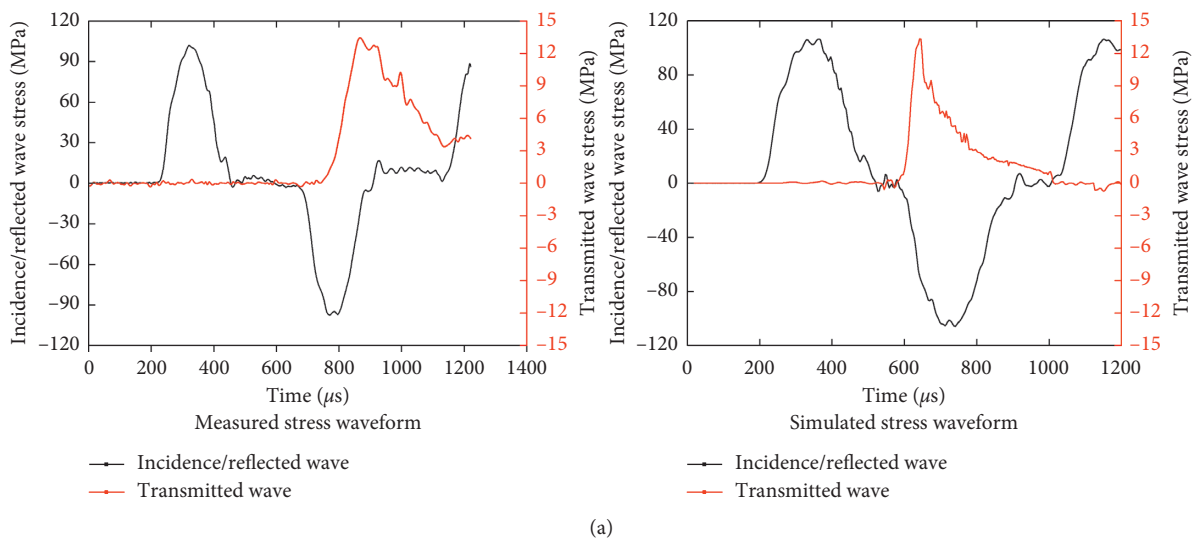


FIGURE 5: Continued.

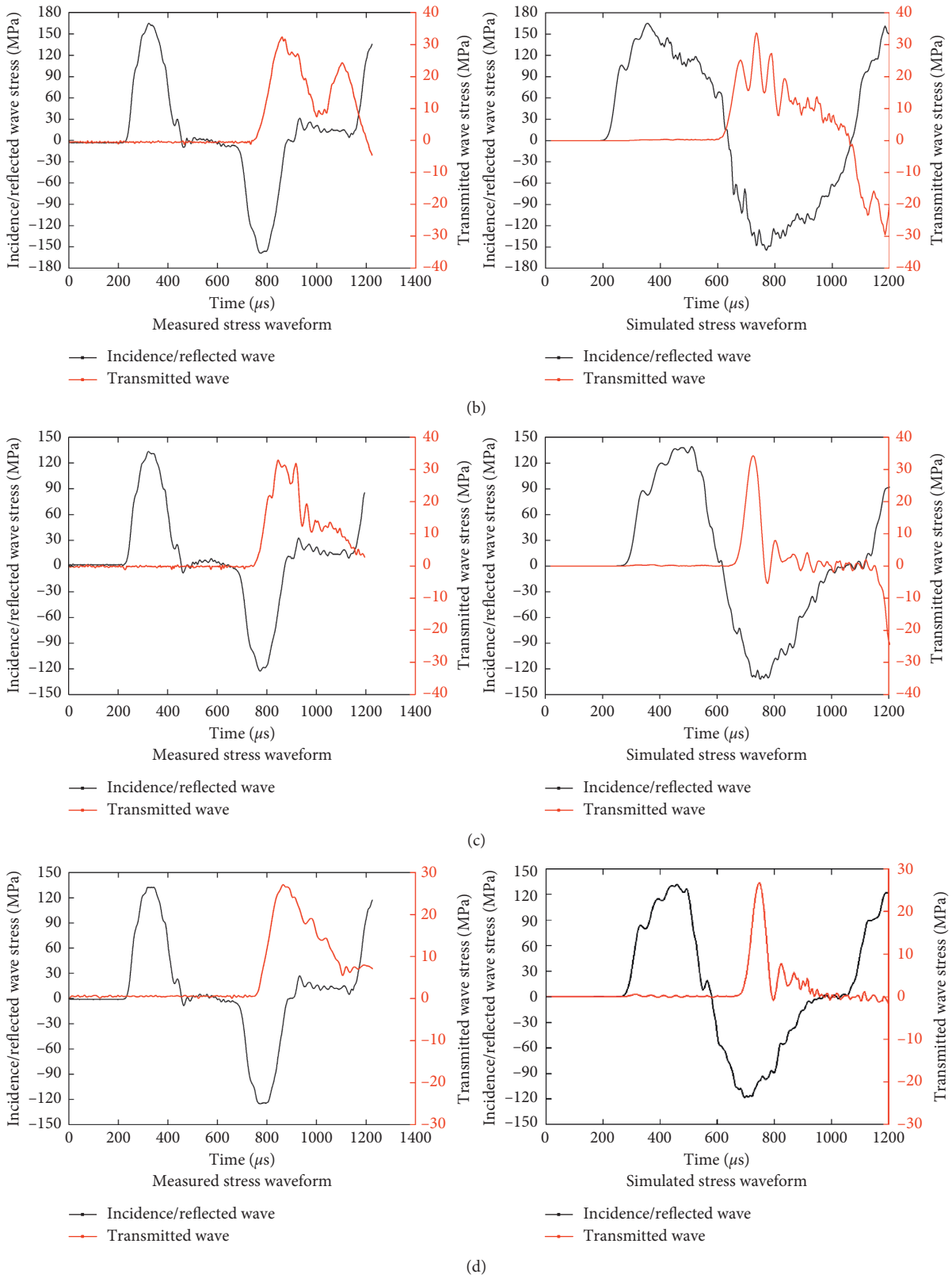


FIGURE 5: Stress waves of the incident bar and transmission bar at different bullet speeds: (a) 5.008 (m/s); (b) 7.671 (m/s); (c) 6.660 (m/s); (d) 5.880 (m/s).

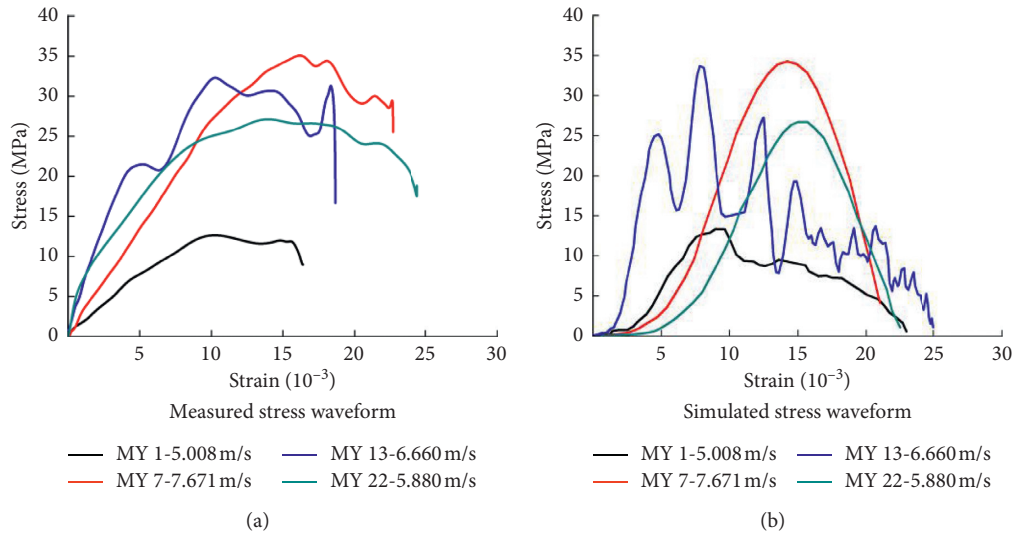


FIGURE 6: Stress-strain curve: (a) measured; (b) simulated.

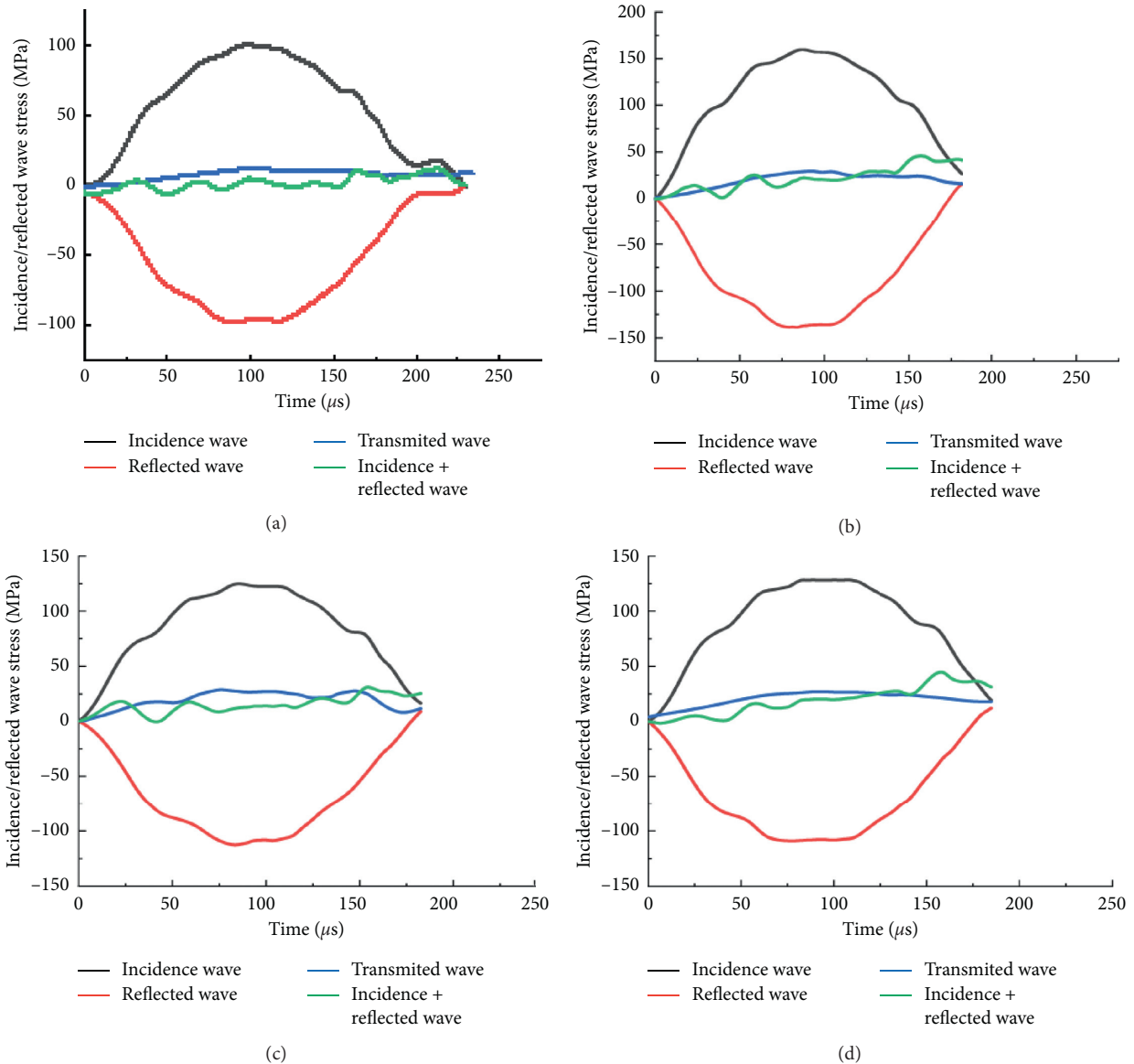


FIGURE 7: Dynamic stress equilibrium curves: (a) bullet speed = 5.008 (m/s); (b) bullet speed = 7.671 (m/s); (c) bullet speed = 6.660 (m/s); (d) bullet speed = 5.880 (m/s).

stress balance of each sample is relatively good in the whole loading process.

4.3. Analysis of the Failure Process of the Combined Coal and Rock. High-speed photography is utilized to capture the failure process of the combined coal-rock SHPB test. Moreover, the impact process of the combined coal-rock is analyzed and compared with the simulated combined coal-rock failure process, as shown in Figure 8.

Figure 8(a) indicates that, for the combined coal-rock of 1 : 1 : 1 affected at a speed of 5.008 m/s, the stress waves reach the sample at $t = 395.96 \mu\text{s}$ and the coal is damaged by the compression shearing. When $t = 545.9 \mu\text{s}$, the rear end of the sandstone is subjected to the axial and tensile cracking and the damage is completed at $t = 800.94 \mu\text{s}$. During the whole test, the coal edge is sprayed in the radial direction, while the sandstone is maintained a certain degree of integrity. It should be indicated that this situation is in good agreement with the actual test process. Figure 8(b) indicates that, for the 2 : 1 : 1 combined coal-rock with an impact velocity of 7.671 m/s, the stress waves reach the sample at $t = 398.93 \mu\text{s}$ and the coal is damaged by the compression and shear. When $t = 434.96 \mu\text{s}$, the sandstone is subjected to the axial and tensile cracking and damage is completed at $t = 788.97 \mu\text{s}$. Throughout the experiment, the edge of the coal is sprayed radially along the compression shear, while the sandstone is maintained in a good integrity. In the actual experimental failure process, the sandstone instability produces radial cracks at the front end. Simulation result indicates that the rear sandstone creates radial cracks. The analysis shows that the front-end sandstone has cracks and creates radial cracks, when it is subjected to impact loads. Furthermore, Figure 8(c) shows that, for the 1 : 1 : 2 combined coal-rock with an impact velocity of 6.660 m/s, the stress waves reach the sample at $t = 392.92 \mu\text{s}$ and the coal is damaged by compression shearing. When $t = 431.99 \mu\text{s}$, the rear end sandstone is subjected to the axial cracking and tensile cracking and the damage is completed at $t = 761.98 \mu\text{s}$. During the whole test, the edge of the coal is sprayed radially in the radial direction, while the sandstone is maintained in a good integrity. This condition is in a good agreement with the actual experimental failure process. Finally, Figure 8(d) illustrates that, for the 1 : 2 : 1 combination coal-rock with an impact velocity of 5.880 m/s, the stress waves reach the sample at $t = 389.99 \mu\text{s}$ and the coal is damaged by the compression shearing. When $t = 404.99 \mu\text{s}$, the rear end sandstone is subjected to the axial and tensile cracking and the damage was completed at $t = 779.94 \mu\text{s}$. During the test, the edge of the coal is sprayed radially in the radial direction and the sandstone is maintained in a certain degree of integrity. Due to the equipment failure, the experimental process cannot be captured in this case. In addition, due to parameter settings, some element failures are lost and can be further simulated and verified later.

It is observed that, in the combined coal-rock SHPB impact test, the coal body first suffers damage and the sandstone produces the tensile damage. These damages are mainly caused by the coal body damage and have no clear

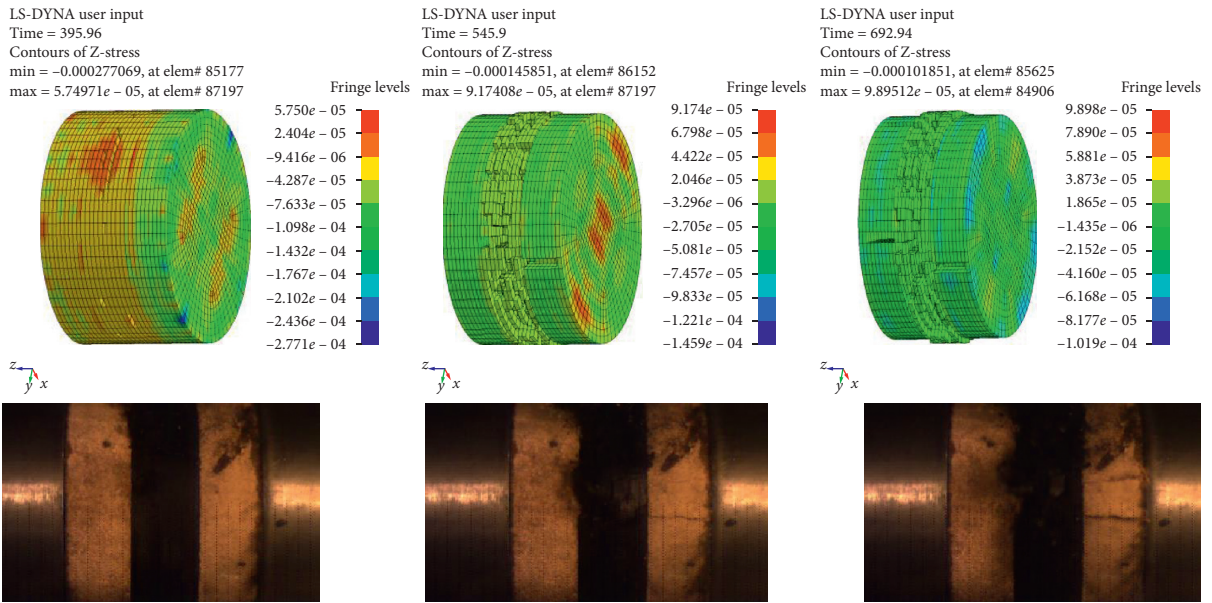
correlation with the impact speed and the combination mode. The main failure modes of coal bodies are compression and shear failure, and the failure modes of sandstone are tensile failure along the axial direction. Furthermore, the edge of the coal is sprayed radially in the radial direction. It is found that the greater the impact velocity, the more severe the damage. Tensile damage occurs in the back-end sandstone, and the front sandstone still maintains good integrity.

5. Case Simulation

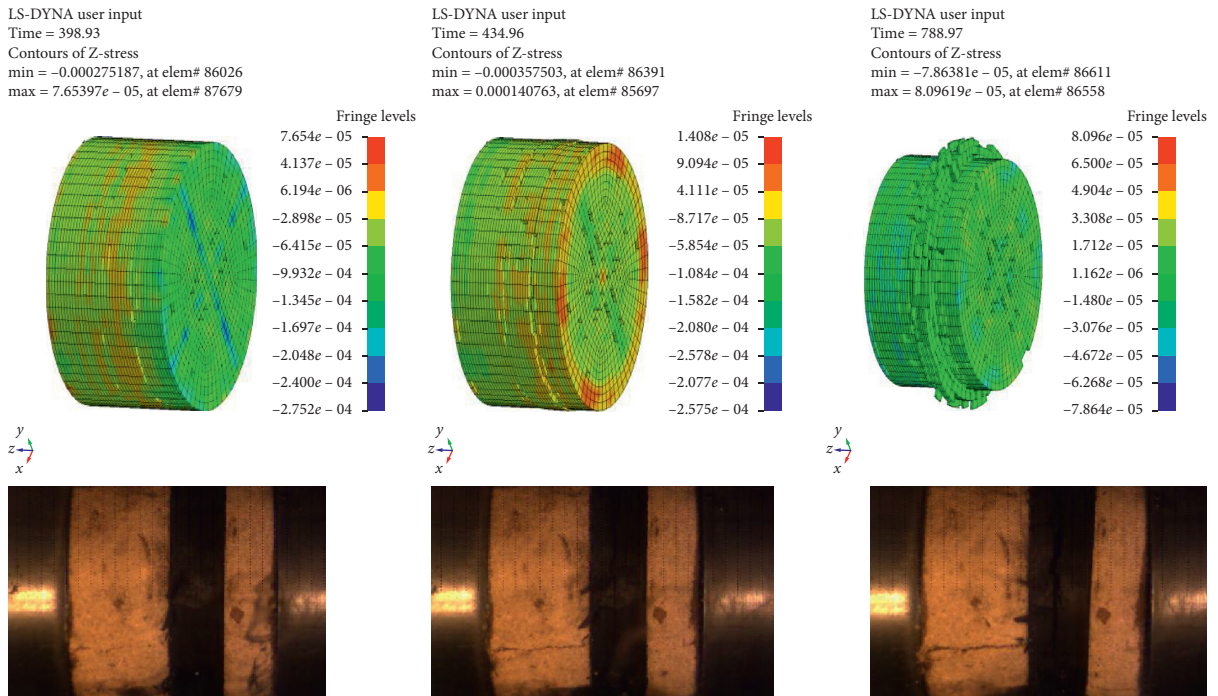
Shenling Group Hongling coalmine is located in Nanhong Village, Honglingbao Town, Sujiatun District, Shenyang City. The coalfield strata of the minefield are intercontinental sediments of sea and land, and the lithology is composed of sandstone and mudstone interbeds. The average dip angle of the coalfield in the minefield is 30° . It should be indicated that the Hongling coalmine is a mine with coal and gas outburst. The mine development method is a multilevel partitioning method for the main well. The ventilation method is the central diagonal type. The coal is mined by the blasting method, and the punching and blasting technique is utilized for the excavation. Over the years, there have been more than 140 coal and gas outburst accidents in the Hongling coalmine, including 15 accidents caused by the coal seam of tunnel exposing (more than 10% of total mine accidents). Moreover, among 55 casualties of the Hongling coalmine, 43 miners died in the coal seam of tunnel exposing, which accounts for almost 80% of the total casualties, due to outstanding accidents. Moreover, the largest coal and gas outburst in the Hongling coalmine was a prominent accident that occurred after the 12th coal seam of the tunnel exposing on June 20, 1996. The outstanding coal volume is 5390 t, which is a large-scale prominent. The forehead coal seam is 4.2 m thick, and the inclination angle is 37° [38]. Figure 9 shows a cross-sectional view of the coal and gas outburst accidents.

5.1. Numerical Simulation Model. Taking the largest coal and gas outburst in the Hongling coalmine as an example, Ansys and LS-DYNA finite element software are used to visualize the stress distribution law for the surrounding rocks during the outburst process. The length, width, and height of the calculation model are set to 50 m, 3 m, and 50 m, respectively. Moreover, the thickness of the coal seam and the inclination angle are set to 5 m and 30° , respectively. Figure 10 indicates that the roadway is 40 m long, 3 m wide, and 3 m high. The left- and right-side boundaries of the model are constrained by the X-direction, while the bottom boundary is confined to the Y-direction. The applied ground stress to the model is obtained by the field measurement. The initial horizontal direction ground stress is $\sigma = 18 \text{ MPa}$.

5.2. Variation Law of the Outburst Stress Field. In underground explosive operations, the shock wave generated by the blasting transmits the large amount of the blasting energy to the surrounding area. In severe cases, this energy can cause

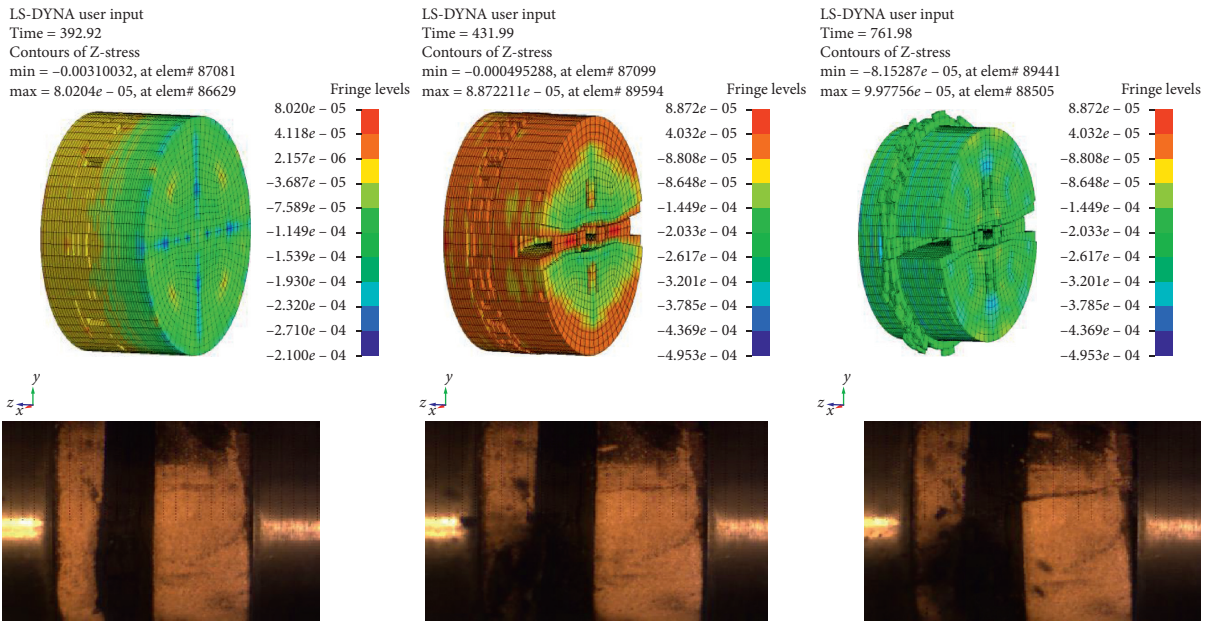


(a)

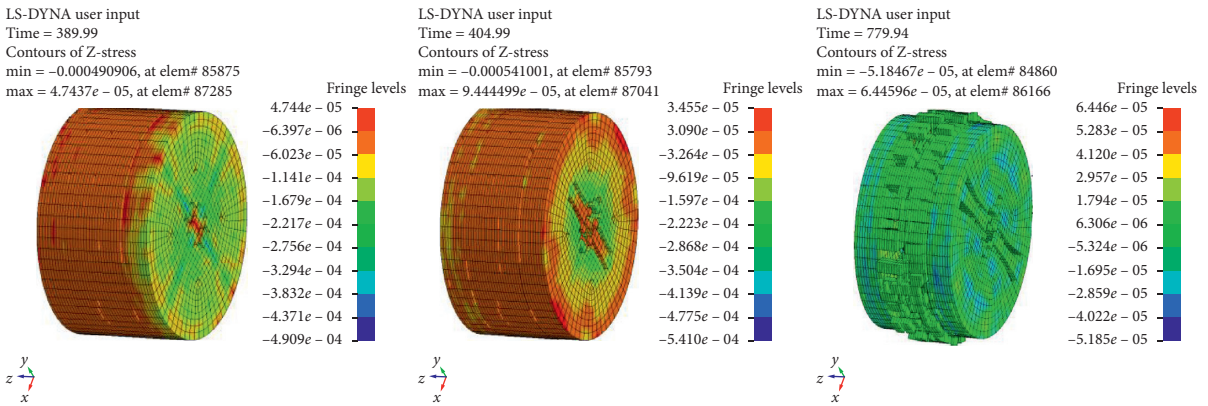


(b)

FIGURE 8: Continued.



(c)



(d)

FIGURE 8: Dynamic change process under coal impact damage: (a) bullet speed = 5.008 (m/s); (b) bullet speed = 7.671 (m/s); (c) bullet speed = 6.660 (m/s); (d) bullet speed = 5.880 (m/s).

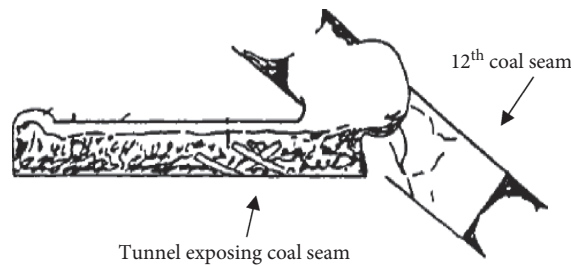


FIGURE 9: Sectional view of “6.20” outburst incident.

protrusion in the process of the coal seam of the tunnel exposing. The stress wave disturbance caused by the excavation blasting is also simplified into a semisinusoidal pulse. The dynamic stress-strain curve obtained by the coal-fired SHPB test is taken as the maximum peak of the half-sinusoidal pulse amplitude of 20 MPa. The constitutive parameters of coal materials and sandstone are presented in Tables 2 and 3,

respectively. The numerical simulation is used to realize the visualization of the prominent dynamic disasters of the coal seam of the tunnel exposing. The obtained results from the numerical simulation are shown in Figure 11.

Figure 11 shows the variation in the coal seam stress of the tunnel exposing. It is observed that when $t = 2.8 \mu s$, the disturbing stress wave contacts the coal seam and the coal

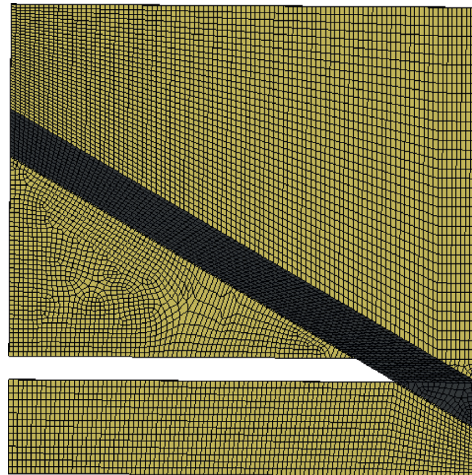


FIGURE 10: Numerical model of the process of the coal seam of the tunnel exposing.

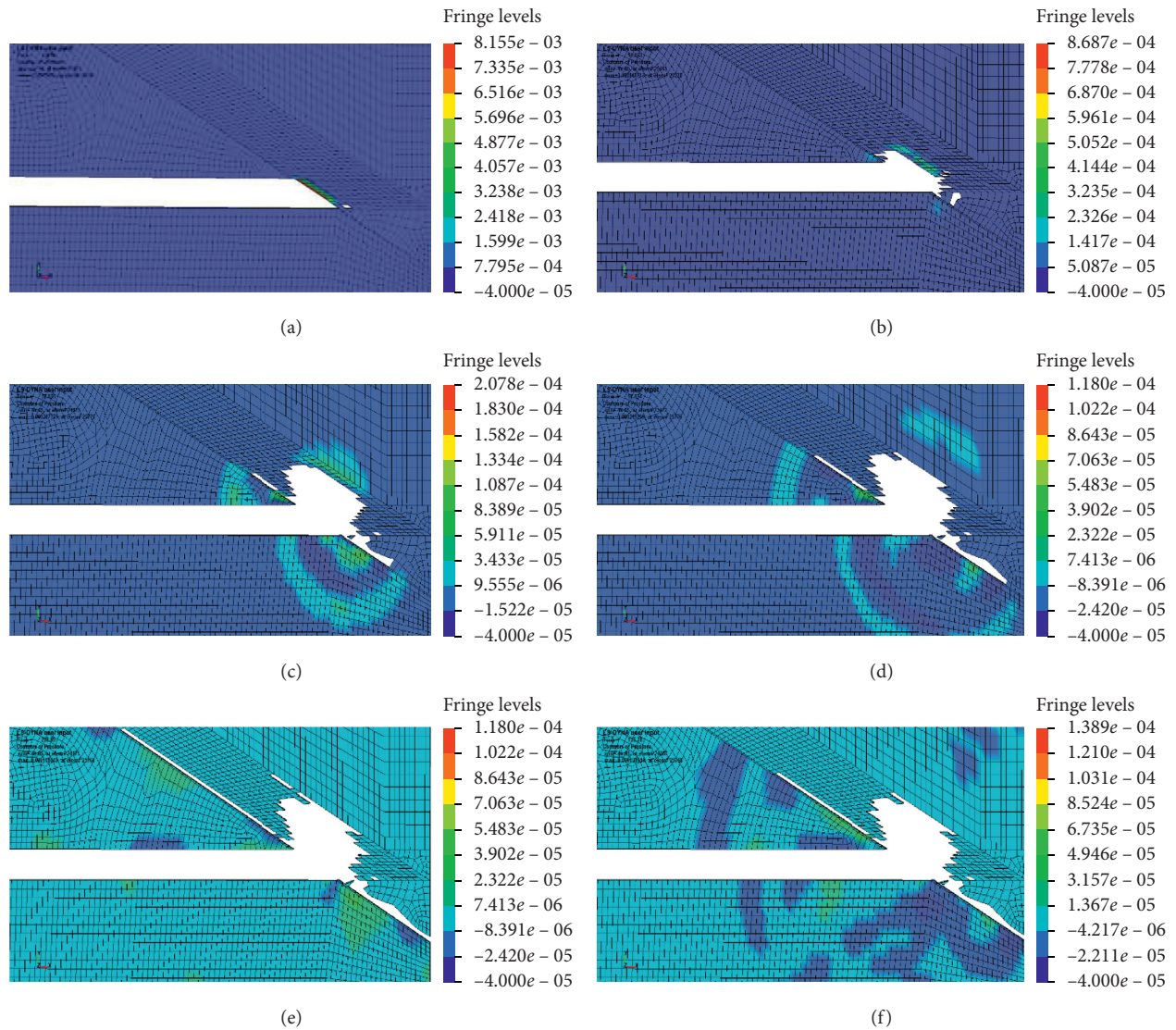


FIGURE 11: The process of the coal seam of the tunnel exposing: (a) $t = 2.8$ (μs) (pressure: Min=-4e-05, at elem. #25761; Max=0.00815452, at elem. #32265); (b) $t = 14.8$ (μs) (pressure: Min=-4e-05, at elem. #25765; Max=0.000868713, at elem. #29220); (c) $t = 38.8$ (μs) (pressure: Min=-4e-05, at elem. #24173; Max=0.000207775, at elem. #25776); (d) $t = 56.9$ (μs) (pressure: Min=-4e-05, at elem. #23472; Max=0.000219299, at elem. #25776); (e) $t = 116.8$ (μs) (pressure: Min=-4e-05, at elem. #24387; Max=0.000138914, at elem. #25768); (f) $t = 218.9$ (μs) (pressure: Min=-4e-05, at elem. #24171; Max=0.000118043, at elem. #25768).

seam begins to crack. Moreover, it is found that when $t = 14.8 \mu\text{s}$, the coal seam is destroyed by the compressive stress wave. As the compressive stress wave continues to expand deep inside the coal seam, the crack gradually expands, the coal seam is notched at $t = 38.8 \mu\text{s}$, and the stress propagates in the rock stratum in three directions. When $t = 116.8 \mu\text{s}$, the gap size generated by the coal seam decreases, and then, it increases with the stress waves transmission. Finally, when $t = 218.9 \mu\text{s}$, a large cavity is formed deep in the coal seam with the increase in the notch.

Figure 11 indicates that the coal seam and the surrounding rock mass are in a weak equilibrium state, when the coal is uncovered. It is found that the disturbance caused by the excavation blasting, instantaneously, destroys the equilibrium state, and the coal body loses the lateral support. It should be indicated that the strength of the coal body is much lower than the strength of the rock mass. Therefore, in the coal body near the exposed surface, microfracture occurs due to the unloading action. With the expansion of the microfracture in the coal body, the high-stress zone advances to the deep part of the coal body and the elastic potential in the coal seam is immediately released. Coal is thrown toward the roadway under the crustal stress, and it is called coal outburst. Then, when the stress of coal and rock returns to the equilibrium state, the appearance of coal outburst stops. It is observed that the obtained outburst shape by the simulation results (Figure 11) agrees well with the results of the field investigation after the outburst (Figure 9). Furthermore, it is found that the bursting hole has a small cavity and the bursting hole expands along the interface between the coal body and the top and bottom plates in the horizontal and uphill directions.

6. Conclusions

In the present work, the constitutive model of the rock coal HJC is applied in the finite element software (LS-DYNA) to simulate the combined coal-rock SHPB test. The stress wave oscillation phenomenon and damage process of the specimen during the impact test of the combined coal-rock are simulated to construct the stress waveform. The present study shows that the simulation results have good similarity with those from the experiment. It is concluded that the parameters for the simulation are properly selected. Furthermore, the conclusions of this study are as follows:

- (1) The failure mode of the coal body is mainly due to the compression and shear failure. The failure mode of the sandstone is mainly originated from the tensile failure along the axial direction, which is mainly caused by the coal body damage. It is found that this failure does not have clear correlation with the impact velocity and material combination.
- (2) During the destruction process, the edge of the coal is sprayed radially in the radial direction. It is found that the greater the impact velocity, the more severe the damage, while the sandstone remains intact.

- (3) Comparing the simulation results with the experimental results, the HJC constitutive model of coal and rock can reproduce the dynamic process of coal and rock under impact.
- (4) The dynamic constitutive model parameters of the coal and sandstone HJC are applied to the numerical simulation model of the coal seam of the tunnel exposing. Processes of the coal protruding and the stress change are presented. It is found that the simulation results are in a good agreement with the results of the on-site investigation after the outburst. These results are important for further understanding the mechanism of the protruding coal in the coal seam of the tunnel exposing.

Data Availability

The data used to support the findings of this study are available from the corresponding author upon request.

Conflicts of Interest

The authors declare that they have no conflicts of interest.

Acknowledgments

This research was supported by the National Natural Science Foundation of China (51404277) and the Fundamental Research Funds for the Central Universities (2020YQAQ01 and 2020YJSAQ16).

References

- [1] X. Li, F. Pan, H. Li, M. Zhao, L. Ding, and W. Zhang, "Prediction of rock-burst-threatened areas in an island coal face and its prevention: a case study," *International Journal of Mining Science and Technology*, vol. 26, no. 6, pp. 1125–1133, 2016.
- [2] N. Wang, Y. Q. Xu, D. Y. Zhu, N. Wang, and B. F. Yu, "Acoustic emission and failure modes for coal-rock structure under different loading rates," *Advances in Civil Engineering*, vol. 2018, Article ID 9391780, 11 pages, 2018.
- [3] C. Mark and M. Gauna, "Evaluating the risk of coal bursts in underground coal mines," *International Journal of Mining Science and Technology*, vol. 26, no. 1, pp. 47–52, 2016.
- [4] H. P. Xie, H. W. Zhou, J. F. Liu, and D. J. Xue, "Mining-induced mechanical behavior in coal seams under different mining layouts," *Journal of China Coal Society*, vol. 36, pp. 1067–1074, 2011.
- [5] X. S. Liu, Y. L. Tan, J. G. Ning, Y. W. Lu, and Q. H. Gu, "Mechanical properties and damage constitutive model of coal in coal-rock combined body," *International Journal of Rock Mechanics and Mining Sciences*, vol. 110, pp. 140–150, 2018.
- [6] W. Y. Guo, F. H. Yu, Y. L. Tan, and T. B. Zhao, "Experimental study on the failure mechanism of layer-crack structure," *Energy Science & Engineering*, vol. 7, no. 6, pp. 2351–2372, 2019.
- [7] Y. Chen, J. Zuo, D. Liu, and Z. Wang, "Deformation failure characteristics of coal-rock combined body under uniaxial compression: experimental and numerical investigations,"

- Bulletin of Engineering Geology and the Environment*, vol. 78, no. 5, pp. 3449–3464, 2019.
- [8] F. Q. Gong, H. Ye, and Y. Luo, “Rate effect on the burst tendency of coal-rock combined body under low loading rate range,” *Journal of China Coal Society*, vol. 42, no. 11, pp. 2852–2860, 2017.
- [9] F. Q. Gong, H. Ye, and Y. Luo, “The effect of high loading rate on the behaviour and mechanical properties of coal-rock combined body,” *Shock and Vibration*, vol. 2018, Article ID 4374530, 9 pages, 2018.
- [10] Z. H. Zhao, W. M. Wang, and J. X. Yan, “Strain localization and failure evolution analysis of soft rock-coal-soft rock combination model,” *Journal of Applied Sciences*, vol. 13, no. 7, pp. 1094–1099, 2013.
- [11] B. Fu, Z. H. Zou, Y. X. Wang, S. Liu, and Y. C. Xiao, “Numerical simulation of different combination of coal and rock sample mechanics and acoustic emission characteristics,” *Journal of Nanjing University of Science and Technology*, vol. 4, p. 18, 2016.
- [12] S. S. Hu, “SHPB technique,” *Ordnance Material Science and Engineering*, vol. 11, pp. 42–49, 1991.
- [13] P. Marco, S. George, and B. Norbert, “Development of a Hopkinson bar apparatus for testing soft materials: application to a closed-cell aluminum foam,” *Materials*, vol. 9, no. 1, p. 27, 2016.
- [14] A. S. Yousef, A. Tarek, and A. Saleh, “Rate dependent behavior and modeling of concrete based on SHPB experiments,” *Cement and Concrete Composites*, vol. 55, pp. 34–44, 2015.
- [15] A. Gavrus, F. Bucur, A. Rotariu, and S. Cananau, “Mechanical behavior analysis of metallic materials using a Finite Element modeling of the SHPB test, a numerical calibration of the bar’s elastic strains and an inverse analysis method,” *International Journal of Material Forming*, vol. 8, no. 4, pp. 567–579, 2015.
- [16] S.-H. Wang, C.-S. Huang, W.-S. Lee et al., “Impact deformation behavior of duplex and superaustenitic stainless steels welds by split Hopkinson pressure bar,” *Metals and Materials International*, vol. 15, no. 6, pp. 1007–1015, 2009.
- [17] P. Liu, X. Han, D. Hu, and C. Jiang, “Sensitivity and uncertainty analysis of SHPB tests for concrete materials,” *International Journal of Applied Mechanics*, vol. 8, p. 8, 2016.
- [18] Y. X. Zhao, H. Xiao, and Y. Q. Huang, “Dynamic split tensile test of Brazilian disc of coal with split Hopkinson pressure bar loading,” *Journal of China Coal Society*, vol. 39, no. 2, pp. 286–291, 2014.
- [19] J. Y. Xu, J. Liu, Z. W. Li, E. L. Bai, and W. B. Ren, “Impact mechanical properties of concrete at and after exposure to high temperature,” *Journal of Building Materials*, vol. 16, pp. 45–49, 2013.
- [20] X. L. Li, D. S. Liu, M. D. Feng, S. L. Li, and Z. G. Yan, “Dynamic mechanical properties of concrete materials subjected to passive confining pressure produced by a steel sleeve,” *Explosion and Shock Waves*, vol. 5, no. 2, 2009.
- [21] M. L. Doan and A. Billi, “High strain rate damage of Carrara marble,” *Geophysical Research Letters*, vol. 28, pp. 1066–1073, 2011.
- [22] X. Zhang, Y.-W. Chiu, H. Hao, A. Hsieh, N. Salter, and J. Cui, “Dynamic compressive material properties of clay bricks at different strain rates,” *Construction and Building Materials*, vol. 192, pp. 754–767, 2018.
- [23] F.-Q. Gong, X.-F. Si, X.-B. Li, and S.-Y. Wang, “Dynamic triaxial compression tests on sandstone at high strain rates and low confining pressures with split Hopkinson pressure bar,” *International Journal of Rock Mechanics and Mining Sciences*, vol. 113, pp. 211–219, 2019.
- [24] T. J. Holquist, G. R. Johnson, and W. H. Cook, “A computational constitutive model for concrete subjected to large strains, high strain rate, and high pressures,” *14th International Symposium on Ballistics*, vol. 9, pp. 591–600, 1993.
- [25] B. J. Xie, *Experimental research on characteristics of coal impact damage dynamics and magnetic field*, PhD Thesis, China University of Mining and Technology, Beijing, China, 2013.
- [26] C. W. Li, J. G. Wang, B. J. Xie, P. Hu, and C. Wang, “Numerical analysis of split Hopkinson pressure bar test with passive confined pressure for coal,” *Journal of Mining and Safety Engineering*, vol. 11, pp. 18–21, 2014.
- [27] C. W. Li, J. G. Wang, B. J. Xie, and Y. F. Sun, “Numerical simulation of SHPB tests for coal by using HJC model,” *Journal of Mining & Safety Engineering*, vol. 33, no. 1, pp. 158–164, 2016.
- [28] Y. Yang, *Experimental study on dynamic mechanical properties of rock under low temperature*, PhD Thesis, China University of Mining & Technology, Beijing, China, 2016.
- [29] X. B. Li, T. S. Lok, and J. Zhao, “Dynamic characteristics of granite subjected to intermediate loading rate,” *Rock Mechanics and Rock Engineering*, vol. 38, no. 1, pp. 21–39, 2005.
- [30] Y. X. Zhou, K. Xia, X. B. Li et al., “Suggested methods for determining the dynamic strength parameters and mode-I fracture toughness of rock materials,” *International Journal of Rock Mechanics and Mining Sciences*, vol. 49, no. 1, pp. 105–112, 2012.
- [31] B. J. Xie and Z. Yan, “Dynamic mechanical constitutive model of combined coal-rock mass based on overlay model,” *Journal of China Coal Society*, vol. 44, no. 02, pp. 463–472, 2019.
- [32] J. H. Liu, J. L. Dou, and Y. C. Liu, “The model of specimen transverse inertia influence on testing result of dynamic character of rock,” *Key Engineering Materials*, vol. 462–463, pp. 1056–1061, 2011.
- [33] E. D. H. Davies and S. C. Hunter, “The dynamic compression testing of solids by the method of the split Hopkinson pressure bar,” *Journal of the Mechanics and Physics of Solids*, vol. 11, no. 3, pp. 155–179, 1963.
- [34] M. D. Feng, Y. J. Peng, Y. Q. Liu, H. C. Niu, and R. Li, “Study on SHPB technique,” *Progress in Geophysics*, vol. 21, no. 1, pp. 273–278, 2006.
- [35] B. J. Xie, X. Y. Wang, and P. Y. Lu, “Dynamic properties of bedding coal and rock and the SHPB testing for its impact damage,” *Journal of Vibration and Shock*, vol. 36, no. 21, pp. 117–124, 2017.
- [36] S. Jiang, M. Huang, J. W. Zhan, and X. D. Zhang, “Numerical simulation on the SHPB test of argillaceous siltstone by using the LS-DYNA,” *Nonferrous Metals(Mine Section)*, vol. 68, no. 2, pp. 54–58, 2016.
- [37] D. J. Frew, M. J. Forrestal, and W. Chen, “Pulse shaping techniques for testing brittle materials with a split Hopkinson pressure bar,” *Experimental Mechanics*, vol. 42, no. 1, pp. 93–106, 2002.
- [38] Z. Q. Zhao, J. X. Jin, and J. C. Shen, “Promotion characteristics and induced outburst mechanism of coal plastic zone in rock cross-cut coal uncovering,” *Chinese Journal of Rock Mechanics and Engineering Sciences*, vol. 38, no. 2, pp. 343–352, 2019.